



Cite as

Nano-Micro Lett.
(2021) 13:68

Efficient Two-Dimensional Perovskite Solar Cells Realized by Incorporation of $\text{Ti}_3\text{C}_2\text{T}_x$ MXene as Nano-Dopants

Xin Jin¹, Lin Yang¹, Xiao-Feng Wang¹ ✉

Received: 16 November 2020

Accepted: 5 January 2021

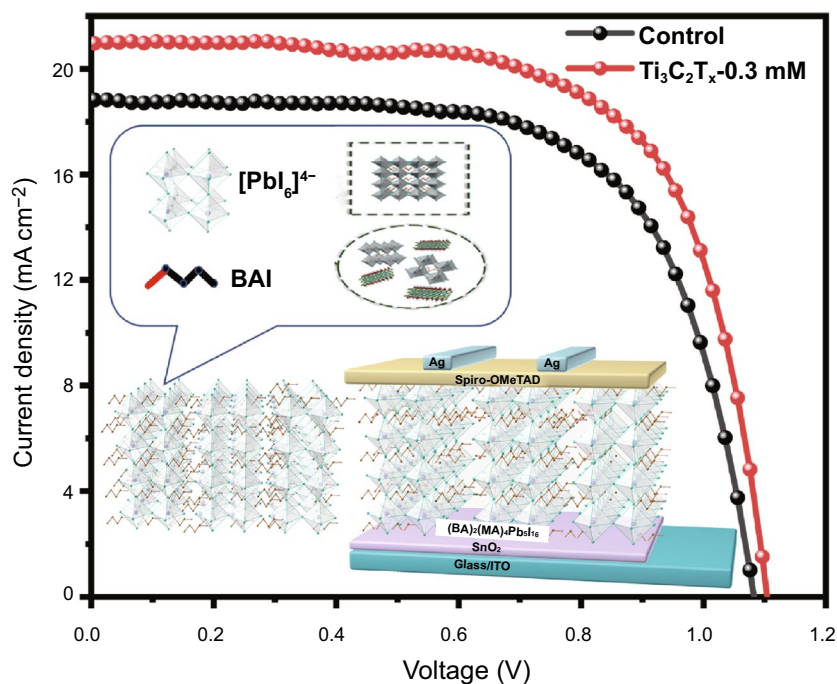
Published online: 11 February 2021

© The Author(s) 2021

HIGHLIGHTS

- 2D $\text{Ti}_3\text{C}_2\text{T}_x$ MXene nanosheets with high electrical conductivity and mobility were employed as a nanosized additive to prepare 2D perovskite films.
- Doping of $\text{Ti}_3\text{C}_2\text{T}_x$ nanosheets can passivate the defects on the perovskite films surface and accelerate charge transfer process in vertical direction.
- Enhanced crystallinity and orientation of the perovskite films result in a significant increase in short-circuit current density and power conversion efficiency.

ABSTRACT Two-dimensional (2D) perovskites solar cells (PSCs) have attracted considerable attention owing to their excellent stability against humidity; however, some imperfectness of 2D perovskites, such as poor crystallinity, disordered orientation, and inferior charge transport still limit the power conversion efficiency (PCE) of 2D PSCs. In this work, 2D $\text{Ti}_3\text{C}_2\text{T}_x$ MXene nanosheets with high electrical conductivity and mobility were employed as a nanosized additive to prepare 2D Ruddlesden–Popper perovskite films. The PCE of solar cells was increased from 13.69 (without additive) to 15.71% after incorporating the $\text{Ti}_3\text{C}_2\text{T}_x$ nanosheets with an optimized concentration. This improved performance is attributed to the enhanced crystallinity, orientation, and passivated trap states in the 3D phase that result in accelerated charge transfer process in vertical direction. More importantly, the unencapsulated cells exhibited excellent stability under ambient conditions with $55 \pm 5\%$ relative humidity.



KEYWORDS 2D perovskite solar cells; $\text{Ti}_3\text{C}_2\text{T}_x$ nanosheets; Trap densities; Vertical orientation; Charge transport

Xin Jin and Lin Yang have contributed equally to this work.

✉ Xiao-Feng Wang, xf_wang@jlu.edu.cn

¹ Key Laboratory of Physics and Technology for Advanced Batteries (Ministry of Education), College of Physics, Jilin University, Changchun 130012, People's Republic of China



1 Introduction

Over the last decade, various efforts have been aimed at converting solar energy to electricity through the photovoltaic effect with novel optoelectrical materials. In particular, organic–inorganic halide perovskites show great potential as excellent light-absorbing materials for photovoltaic devices [1–4]. Thus far, the power conversion efficiencies (PCEs) of organic–inorganic halide perovskite solar cells have been improved from 3.8 to 25.5% through optimization of low-cost solution processing [5, 6]. Although the outstanding photovoltaic performance of perovskite solar cells (PSCs) has attracted worldwide attention, PSCs usually exhibit severe instability to environmental factors, such as moisture, light, and heat, which greatly limits their further commercialization [7]. To address such stability issues, two-dimensional (2D) Ruddlesden–Popper (RP) perovskites with general chemical formula $(A')_2A_{n-1}M_nX_{3n+1}$, where n represents the number of layers of inorganic lead iodide slabs, A' , A , M , and X are a bulky long-chain organic spacer, a monovalent cation, a divalent metal cation, and a halide anion, respectively, have proven to be promising [8–11]. 2D RP perovskites are more thermally rigid, with larger cations impeding internal ion movement and allowing sufficient organic groups. That is, these compositions endow the absorber with hydrophobic properties resulting in improved stability in moist environment [12–14]. On the other hand, these structural components are offset by the large exciton binding energy and lower crystallinity [15, 16], which severely affect the separation and transport of carriers and ultimately lead to relatively low current and PCE values.

Current methods for orientation and crystal engineering of 2D RP perovskite films mainly include hot-casting [9], additive-assisted methods, and solvent engineering [17–29]. The hot-casting technique was used to prepare perovskite films, resulting in high-quality films with preferred growth orientation, which facilitates the transfer of charges along the vertical direction of the film; the disadvantage of this approach is that it is difficult to precisely control the temperature. A small amount of Cs^+ doping resulted in a significant efficiency improvement in 2D RP PSCs [22]. More recently, a PCE of 18.04% with a short-circuit current density (J_{sc}) of 17.91 mA cm^{-2} was achieved in a $(\text{BA})_2\text{MA}_4\text{Pb}_5\text{I}_{16}$ 2D RP perovskite solar cell based on a water-assisted crystallization process; this translated into an increase in the J_{sc} (from

17.61 to 19.01 mA cm^{-2}) and PCE (from 13.73 to 15.04%) values of the PSCs [30]. Low current values in 2D PSCs are mainly associated with poor charge transport [18, 31, 32]; therefore, carefully regulating the growth of 2D perovskite films to achieve a better vertical orientation is the key to overcome this problem [23, 33–35]. Despite great advances in the engineering of thin films, the efficiency of 2D RP PSCs is still behind that of their 3D counterparts, especially for the J_{sc} [36], and further work is needed to improve their efficiency to meet the commercialization requirement.

MXenes are 2D transition metal carbides and nitrides with a $M_{n+1}X_nT_x$ composition, obtained by etching the A (Al, Sn, etc.) layer of the MAX phase, where M represents an early transition metal, X represents carbon and/or nitrogen, and T_x indicates surface termination groups (usually $-\text{O}$, $-\text{OH}$, and/or $-\text{F}$) [37]. $\text{Ti}_3\text{C}_2\text{T}_x$, as the first discovered typical MXene, has many excellent properties, including high electrical conductivity, mobility, hydrophilicity, and flexibility [38], which are widely applied in energy storage, supercapacitors, sensors, catalysis, and electromagnetic interference shielding. In addition, $\text{Ti}_3\text{C}_2\text{T}_x$ has been widely applied as a different component in solar cells. For instance, oxidized $\text{Ti}_3\text{C}_2\text{T}_x$ was employed as electrode in dye-sensitized solar cells, resulting in a PCE of 2.66% [39]. Fu et al. [40] reported few-layered $\text{Ti}_3\text{C}_2\text{T}_x$ MXene-contacted Si solar cells with a record PCE of 11.5%. Yu et al. [41] applied $\text{Ti}_3\text{C}_2\text{T}_x$ materials both as electron- and hole-transport layers in organic solar cells and achieved a PCE of 9.06%. We demonstrated the use of UV-ozone-treated $\text{Ti}_3\text{C}_2\text{T}_x$ as electron transport layer (ETL) in PSCs and obtained a highly improved PCE of 17.17% [42]. Moreover, $\text{Ti}_3\text{C}_2\text{T}_x$ was employed as an additive in SnO_2 [43] or $\text{TiO}_2/\text{SnO}_2$ [44] multidimensional ETLs, obtaining a high PCE of more than 18%. Guo et al. [45] reported that $\text{Ti}_3\text{C}_2\text{T}_x$ doping in the $\text{CH}_3\text{NH}_3\text{PbI}_3$ perovskite layer efficiently enhanced the crystal size and charge transfer of the film. Thus, $\text{Ti}_3\text{C}_2\text{T}_x$ MXenes have proven to be promising additives for PCE improvement, highlighting their great potential for application in the field of 2D PSCs, in which $\text{Ti}_3\text{C}_2\text{T}_x$ MXenes remain largely unexplored.

In this study, we for the first time fabricate PSCs employing the 2D $(\text{BA})_2(\text{MA})_4\text{Pb}_5\text{I}_{16}$ RP perovskite absorber in which $\text{Ti}_3\text{C}_2\text{T}_x$ nanosheets were added as a nano-dopant. Systematic analyses showed that the addition of $\text{Ti}_3\text{C}_2\text{T}_x$ nanosheets in the precursor solution led to a homogeneous perovskite film formation during spin-coating process

resulting in spontaneous passivation of grain boundaries. X-ray diffraction (XRD) measurements indicate that the incorporation of an optimal amount of $\text{Ti}_3\text{C}_2\text{T}_x$ nanosheets resulted in an enhanced crystallinity along with a preferential growth perpendicular to the substrate. Meantime, the multiphase coexistence in the 2D perovskite films could be modulated in a preferred order. These characteristics facilitated efficient charge transport, which boost the PCE from 13.69 to 15.71%, as the J_{sc} increases from 18.84 to 20.87 mA cm^{-2} .

2 Experimental Section

2.1 Materials

Lead iodide (PbI_2 , > 99.99%), methylammonium iodide (MAI, > 99.5%), BAI (99.5%), and lithium-bis (trifluoromethanesulfonyl) imide (Li-TFSI, > 99%) were purchased from Xi'an Polymer Light Technology Corp. NH_4SCN was purchased from Aladdin. 2,2',7,7'-tetrakis-(*N,N*-di-*p*-methoxyphenylamino)-9,9'-spirobifluorene (Spiro-OMeTAD, > 99.8%), 4-tert-butyl pyridine (tBP, 96%), and ultra-dry anhydrous *N,N*-dimethylformamide (DMF, 99.8%) and dimethyl sulfoxide (DMSO, 99.7%) were purchased from Sigma-Aldrich. All materials are not further purified before use.

2.2 Preparation of $\text{Ti}_3\text{C}_2\text{T}_x$ MXene Hydrocolloid

The method is the same as our previous report. The 400-mesh uniform Ti_3AlC_2 MAX powder was added into 12 M LiF/9 M HCl solution with continuously stirring for 24 h at room temperature. Specifically, 1.6 g LiF was added to 20 mL 9 M HCl solution at room temperature and stirred for 5 min. Then 1.0 g Ti_3AlC_2 MAX powder was slowly added (about 5 min) to the etchant solution and continuously etched for 24 h at room temperature. After etching process, the obtained acid mixture was repeatedly washed over 6 times with deionized water by centrifugation at 8000 rpm for 5 min until the pH of mixture reached about 6. Finally, the slurry was sonicated for 30 min in an ice bath under argon and centrifuged at 3500 rpm for 1 h to separate the multi-layers. The obtained dark supernatant was the colloid solution of $\text{Ti}_3\text{C}_2\text{T}_x$ nanosheets, which could be used directly

as the additive in 2D perovskite precursor. To confirm and tune the concentration of $\text{Ti}_3\text{C}_2\text{T}_x$ colloid, a quantitative solution was filtered over a 0.22 μm pore sized cellulose membrane and the concentration of $\text{Ti}_3\text{C}_2\text{T}_x$ was determined to be 11.6 mg mL^{-1} by weighing the peeled-off dried film. Moreover, the solution was diluted to 5.8 mg mL^{-1} by adding deionized water and sonicated for 30 min to control the average size to about 200 nm for better using as additive in perovskite precursor.

2.3 Preparation of 2D Perovskite Precursor Solution

The precursor solution of 2D perovskite $\text{BA}_2\text{MA}_4\text{Pb}_5\text{I}_{16}$ ($n=5$) was prepared by mixing BAI, MAI, PbI_2 , and NH_4SCN in dimethylsulfoxide (DMSO) and dimethylformamide (DMF) solvents (5:5 volume ratio) with a stoichiometric ratio of 2:4:5:2; the concentration of Pb^{2+} in the precursor solution was 1.2 M. Then, $\text{Ti}_3\text{C}_2\text{T}_x$ hydrocolloid (5.8 mg mL^{-1}) was added to the perovskite precursor, at $\text{Ti}_3\text{C}_2\text{T}_x$ concentrations of 0.1, 0.3, 0.5, and 0.7 mM. The solution was stirred for 8 h at 50 °C before use.

2.4 Film Preparation and Device Fabrication

The ITO-coated transparent substrates were cleaned with water, acetone, and alcohol in an ultrasonic bath for 30 min. After drying, the cleaned ITO substrates were treated with UV/ozone for 15 min before use. The SnO_2 colloid was diluted to 3 wt% by mixing with deionized water and spin-coated onto the ITO substrates at 3000 rpm for 30 s, followed by thermal annealing on a hot plate at 150 °C for 30 min and UV/ozone treatment for 15 min. Then, the UV/ozone-treated substrates were rapidly transferred into a glove box filled with argon, where the 2D perovskite films were fabricated by spin coating the precursor solutions onto the substrates at 4000 rpm for 30 s; during the spin coating process, 300 μL toluene was dripped onto the 2D perovskite film, followed by solvent annealing in DMF atmosphere at 100 °C for 10 min. To prepare the samples containing $\text{Ti}_3\text{C}_2\text{T}_x$, different amounts of $\text{Ti}_3\text{C}_2\text{T}_x$ were introduced in the precursor solution. After the 2D perovskite film was cooled down to room temperature, spiro-MeOTAD was spin-coated on the 2D perovskite film at 4000 rpm for 30 s; the coating solution was prepared by dissolving 72.3 mg spiro-MeOTAD in 1 mL anhydrous chlorobenzene with 28.8 μL

tBP and 17.5 μL Li-TFSI (520 mg mL^{-1} acetonitrile) additives. The samples were kept overnight in the dark and dry air at room temperature. Finally, an 80-nm Ag electrode was thermally evaporated on top of spiro-MeOTAD under high vacuum (1×10^{-4} Pa). The active device area was determined as 0.04 cm^2 by overlapping the Ag and ITO electrodes.

2.5 Characterization

2.5.1 Thin Film Characterization

UV/Vis absorption spectra were carried out with a Shimadzu UV-1900 spectrophotometer over wavelength range of 300–900 nm. The XRD patterns were recorded on Bruker D8 X-ray diffractometer with Cu $K\alpha$ radiation ($\lambda = 1.5418 \text{ \AA}$) at room temperature ($25 \text{ }^\circ\text{C}$). The data were collected with a 0.02° step size (2θ) for 0.2 s. Top-view and cross-sectional scanning electron microscopy (SEM) images were acquired by a field emission scanning electron microscope (Hitachi SU8000) with an energy dispersive spectroscopy (EDS) system. The TEM images were recorded using a JEM-2200FS (JEOL). The roughness of perovskite films was characterized by using AFM (5500, Agilent, Santa Clara, CA). Steady photoluminescence (PL) measurements were carried out by RF-6000 spectrophotometer, while TRPL results were acquired by PL spectrometer (Edinburgh Instruments, FLS 920).

2.5.2 Device Characterization

The J – V characteristics of perovskite solar cells were carried out by a Keithley 2400 source meter measurement system with an AM 1.5G filter at an illumination intensity of 100 mW cm^{-2} , while the solar simulator was calibrated with a Si solar cell and the effective area of the cells was confirmed to be 0.04 cm^2 . The EQE spectra were measured using SOFN 7-SCSpecIII equipped with a 100 W Xe arc lamp, a filter wheel, and a monochromator. The EIS measurements of the devices were carried out on a Princeton electrochemical workstation (Parstat Mc Princeton Instruments Co., Ltd., USA); Z-View Analyst software was used to model the Nyquist plots obtained from the impedance measurements.

3 Results and Discussion

3.1 Characterization of $\text{Ti}_3\text{C}_2\text{T}_x$ Nanosheets

$\text{Ti}_3\text{C}_2\text{T}_x$ nanosheets were obtained by etching the original Ti_3AlC_2 powder, as described in the experimental section. To confirm the successful transformation of the raw Ti_3AlC_2 powder into $\text{Ti}_3\text{C}_2\text{T}_x$ nanosheets, samples of Ti_3AlC_2 powder and $\text{Ti}_3\text{C}_2\text{T}_x$ nanosheets were tested by XRD (Fig. 1a). As can be seen in the figure, the disappearance of the strongest diffraction peak of Ti_3AlC_2 (104) is accompanied by a shift of the (002) peak from 9.5° to about 7° , which indicates that the Al layer was successfully etched. The diffraction pattern of the $\text{Ti}_3\text{C}_2\text{T}_x$ nanosheets displays four sharp peaks at approximately 7° , 14° , 22° , and 28° , corresponding to the (002), (004), (006), and (008) facets, respectively, which is consistent with previous reports [43]. For the purpose of mixing the $\text{Ti}_3\text{C}_2\text{T}_x$ nanosheets with the perovskite precursor, smaller sized monolayered $\text{Ti}_3\text{C}_2\text{T}_x$ nanosheets were obtained by another 30 min of sonication, as shown in the SEM and transmission electron microscopy (TEM) images in Fig. 1b, c, respectively. The size distribution results for the monolayer $\text{Ti}_3\text{C}_2\text{T}_x$ nanosheets show an average size of approximately 200 nm (Fig. 1d). In order to apply $\text{Ti}_3\text{C}_2\text{T}_x$ nanosheets in perovskite devices, we incorporated $\text{Ti}_3\text{C}_2\text{T}_x$ hydrocolloid into the precursor solution, at concentrations of 0, 0.1, 0.3, 0.5, and 0.7 mM; in the following, the corresponding samples are labeled as control, $\text{Ti}_3\text{C}_2\text{T}_x$ -0.1 mM, $\text{Ti}_3\text{C}_2\text{T}_x$ -0.3 mM, $\text{Ti}_3\text{C}_2\text{T}_x$ -0.5 mM, and $\text{Ti}_3\text{C}_2\text{T}_x$ -0.7 mM, respectively.

3.2 Photovoltaic Devices Performance

Figure 2a shows an architecture of the present PSCs together with the illustration of introducing $\text{Ti}_3\text{C}_2\text{T}_x$ into the 2D perovskite film. To determine how different $\text{Ti}_3\text{C}_2\text{T}_x$ nanosheet contents affect the photovoltaic performance of 2D $(\text{BA})_2(\text{MA})_4\text{Pb}_5\text{I}_{16}$ perovskite devices, we fabricated devices with an n – i – p planar architecture on the optically transparent electrode consisting of the indium tin oxide (ITO), the SnO_2 electron transporting layer (ETL), the 2D perovskite layer, the Spiro-OMeTAD hole transporting layer (HTL), and the Ag back electrodes. The J – V curves of devices fabricated with the control, $\text{Ti}_3\text{C}_2\text{T}_x$ -0.1 mM,

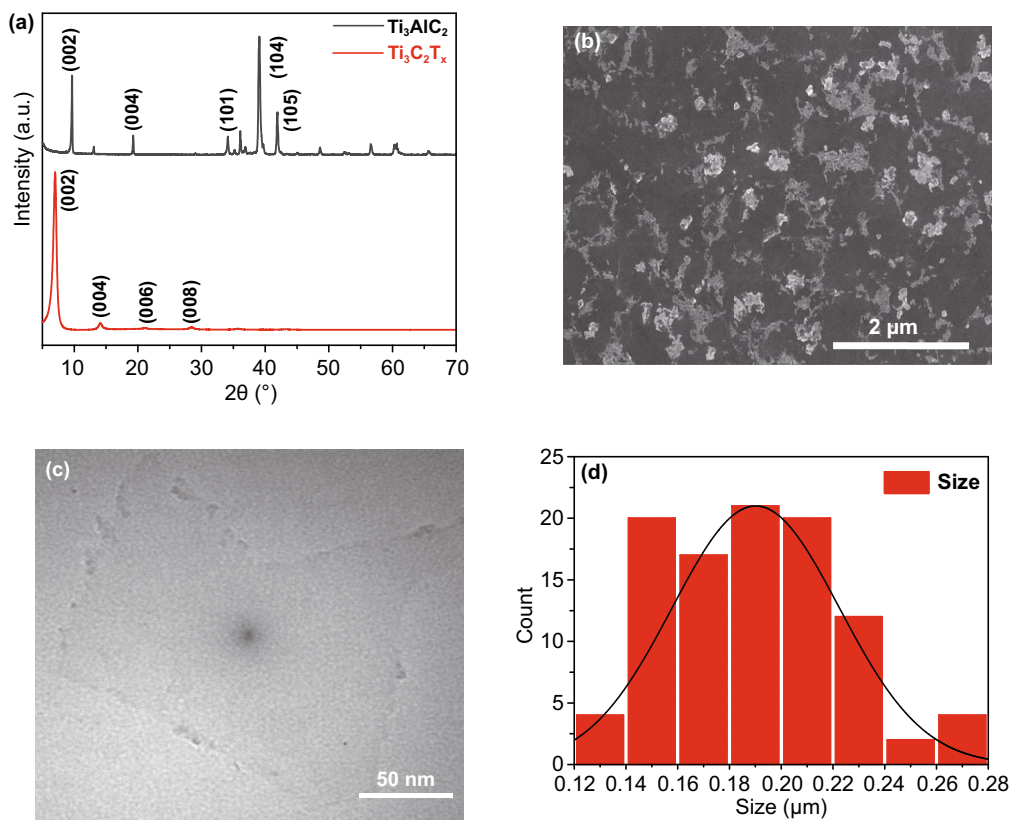


Fig. 1 **a** XRD patterns of raw Ti₃AlC₂ powder and Ti₃C₂T_x nanosheets. **b** SEM and **c** TEM images of monolayer Ti₃C₂T_x nanosheets after sonication. **d** Particle size statistics for monolayer Ti₃C₂T_x nanosheets after sonication

Ti₃C₂T_x-0.3 mM, Ti₃C₂T_x-0.5 mM, and Ti₃C₂T_x-0.7 mM samples are shown in Fig. 2b. Table 1 summarizes the corresponding photovoltaic parameters. Overall, the PCE of the present devices increased and then decreased with increase in the Ti₃C₂T_x content. The increase in the PCE of the devices is mainly attributed to the enhanced current density. In particular, the 2D perovskite device with optimal content of Ti₃C₂T_x-0.3 mM showed markedly increased J_{sc} (20.87 mA cm⁻²), open-circuit voltage (V_{oc}) (1.11 V), and fill factor (FF) (67.84%) values, resulting in a greatly improved PCE of 15.71%, compared to a J_{sc} of 18.84 mA cm⁻², V_{oc} of 1.09 V, FF of 66.7%, and PCE of 13.69% obtained for the control device. Clearly, the addition of Ti₃C₂T_x nanosheets led to a significant improvement in photovoltaic performance. This improvement in the J_{sc} is supported by the external quantum efficiency (EQE) spectrum shown in Fig. 2c. The optimal devices prepared with the Ti₃C₂T_x-0.3 mM sample displayed a remarkable change, which can be explained by the marked light absorption associated with Ti₃C₂T_x doping. Based on the EQE spectra,

the devices prepared with the control and Ti₃C₂T_x-0.3 mM samples had integrated current densities of 19.82 and 17.83 mA cm⁻², respectively, within an error of 5%. More devices were fabricated to confirm the efficiency repeatability of devices incorporating the Ti₃C₂T_x nanosheets. Figure S1 presents statistics of the relevant photovoltaic parameters obtained from more than 20 devices based on different doping amounts of Ti₃C₂T_x nanosheets, showing that the average PCE of Ti₃C₂T_x-0.3 mM was 15.32%, which is much higher than the outstanding reproducibility of the control devices (average PCE = 12.11%). In addition, the photocurrent measured for more than 300 s at a maximum power point (0.80 V) indicates a stable power output, consistent with the J - V curves (Fig. 2d).

3.3 Morphology Characterization

To understand what happened upon additional Ti₃C₂T_x in perovskite layer, atomic force microscopy (AFM) and

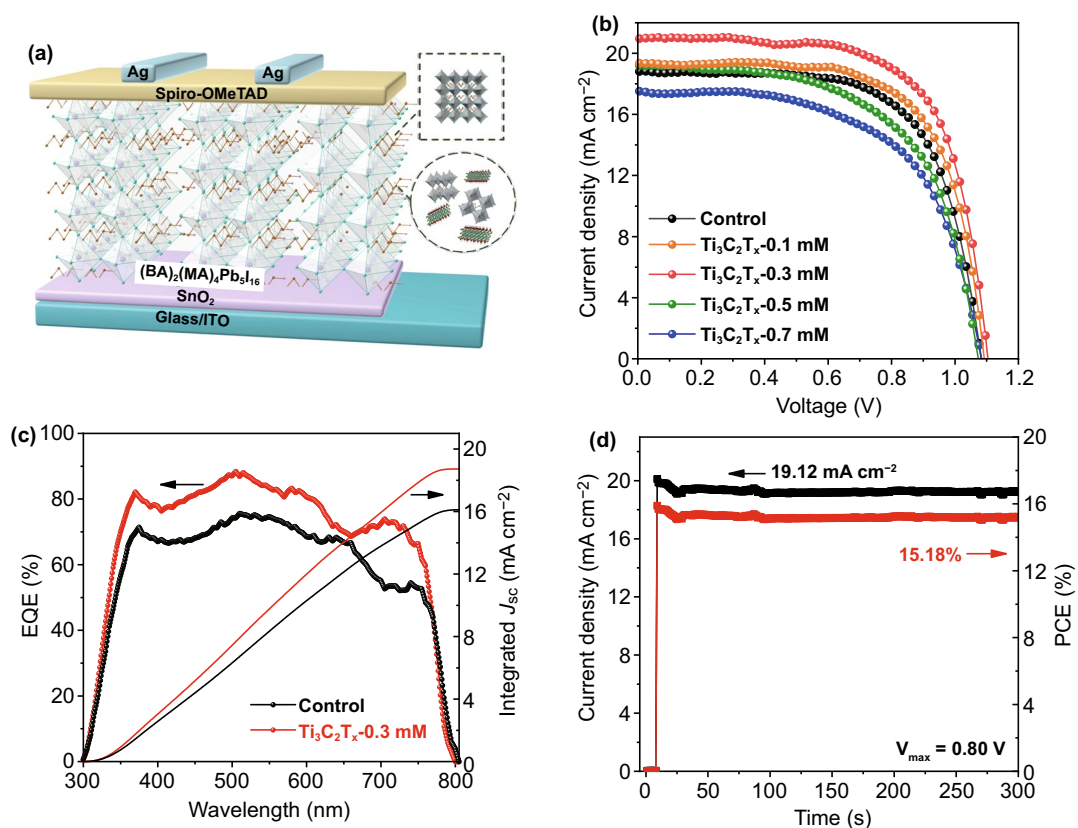


Fig. 2 **a** Schematic diagram of devices with the structure of Glass/ITO/SnO₂/2D perovskite/Spiro-OMeTAD/Ag. **b** *J*-*V* curves of devices with different amounts of Ti₃C₂T_x-doping. **c** EQE spectra and integrated *J*_{sc} of the control and optimized Ti₃C₂T_x-doping devices. **d** Stabilized power output and current density at a constant bias of 0.80 V for the Ti₃C₂T_x-doping devices

Table 1 Photovoltaic parameters of 2D PSCs with/without Ti₃C₂T_x additive

Samples	<i>J</i> _{sc} (mA cm ⁻²)	<i>V</i> _{oc} (V)	FF (%)	PCE (%)
0 mM Ti ₃ C ₂ T _x	18.84	1.09	66.70	13.69
0.1 mM Ti ₃ C ₂ T _x	19.36	1.09	67.39	14.27
0.3 mM Ti ₃ C ₂ T _x	20.87	1.11	67.84	15.71
0.5 mM Ti ₃ C ₂ T _x	19.06	1.07	60.28	12.34
0.7 mM Ti ₃ C ₂ T _x	17.59	1.07	59.39	11.32

SEM were used to inspect the uniformity of the film on the surface of the samples before (control) and after addition of Ti₃C₂T_x. In Fig. 3a, b, the top-view SEM images of Ti₃C₂T_x-0.3 mM show a homogeneous and dense pattern with almost no holes relative to the control film, which displays a highly rough surface and clear cracks. Probably, the small Ti₃C₂T_x nanosheets are spontaneously distributed at the grain boundaries and defects of the intrinsic perovskite film. Such morphological change upon the Ti₃C₂T_x

incorporation must lead to the defect passivation. At other dopant concentrations, observable morphological changes were also observed for Ti₃C₂T_x-0.1 mM, Ti₃C₂T_x-0.5 mM, and Ti₃C₂T_x-0.7 mM (Fig. S3a–c). Increasing the amount of Ti₃C₂T_x in the perovskite layer resulted in a rougher film surface, as further confirmed by AFM (Figs. 3c, d and S3d–f). It is clear that the appropriate amount of Ti₃C₂T_x-0.3 mM could induce a smoother film formation. The root-mean-square (RMS) roughness values of the film surface followed the order Ti₃C₂T_x-0.7 mM > control > Ti₃C₂T_x-0.5 mM > Ti₃C₂T_x-0.1 mM > Ti₃C₂T_x-0.3 mM, which is consistent with the SEM results. In addition, due to the extremely low content of Ti₃C₂T_x relative to PbI₂, we could not use energy-dispersive X-ray spectroscopy (EDS) to confirm the presence of Ti₃C₂T_x along the grain boundaries (below the detection limits of EDS). Therefore, we determined the Ti₃C₂T_x location in the film by increasing its amount to 2 mM. The elemental mappings of Pb, I, and Ti are shown in Fig. S4. The figure shows that the

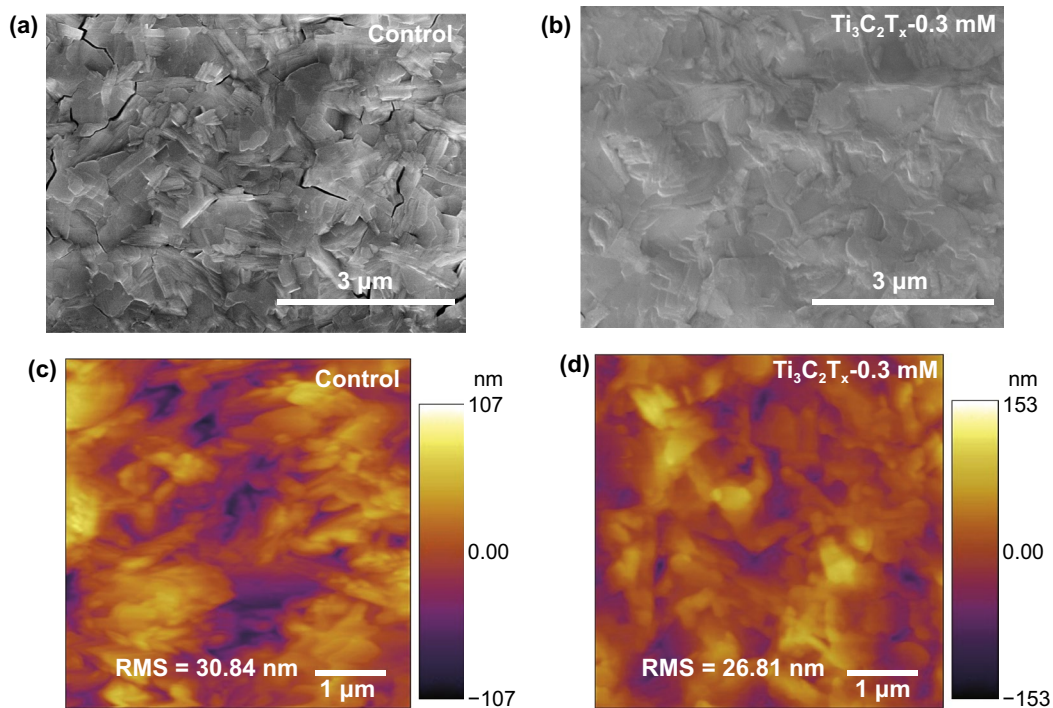


Fig. 3 **a, b** Top-view SEM and **c, d** AFM image of the control and optimized $\text{Ti}_3\text{C}_2\text{T}_x$ -doping perovskite films

Ti species originating from the perovskite precursor were evenly distributed. Based on these observations, it can be concluded that the addition of trace amounts of $\text{Ti}_3\text{C}_2\text{T}_x$ significantly affected the surface morphology of the film. Therefore, the accurate control of the $\text{Ti}_3\text{C}_2\text{T}_x$ content is crucial to improve the photovoltaic performance of the devices.

3.4 Crystalline and Optical Property Analysis

In general, the excellent photovoltaic performance of 2D perovskite devices is strongly dependent on the crystallization and orientation of the film. Figure 4a displays the XRD patterns of the control and $\text{Ti}_3\text{C}_2\text{T}_x$ -0.3 mM perovskite films. The stronger diffraction peaks of $\text{Ti}_3\text{C}_2\text{T}_x$ -0.3 mM indicate a higher crystallinity in comparison with the control film. Both films show two primary diffraction peaks at approximately 14° and 28° , corresponding to the (111) and (202) crystal planes. As previously reported in literature [9], the (202) diffraction peaks indicate 2D perovskite films grown perpendicular to the substrate with vertical orientation, while the (111) crystal planes denote an inclined orientation. In the case of control and $\text{Ti}_3\text{C}_2\text{T}_x$ -0.3 mM perovskite films,

the weaker peak of the (111) crystal plane is accompanied by an enhanced (202) peak, as reflected by (202)/(111) ratios of 0.83 and 1.12, respectively, indicating a better vertical orientation for the $\text{Ti}_3\text{C}_2\text{T}_x$ -0.3 mM perovskite film. As demonstrated by Shi et al. [18] using grazing-incidence wide-angle X-ray scattering (GIWAXS), this property promotes the rapid transport of carriers in 2D perovskite films, leading to an increased current. Furthermore, it is worth noting that the overall XRD peaks of the $\text{Ti}_3\text{C}_2\text{T}_x$ -based film slightly shifted toward lower diffraction angles, which can be attributed to the expansion of the cells by $\text{Ti}_3\text{C}_2\text{T}_x$ doping. 2D perovskite films have a multiphase nature, and the presence of the characteristic peaks of (111) and (202) planes is likely a consequence of multiphase coexistence [46]. Therefore, the above peak shifts may also be related to the distribution of phases, as discussed below.

2D perovskite films often possess multiple phases due to quantum-well structures [47], as shown by the absorption spectra in Fig. 4b. Multiple absorption peaks appear in the spectra of both control and $\text{Ti}_3\text{C}_2\text{T}_x$ -0.3 mM films, such as those at 567, 598, 634, and 775 nm, corresponding to the perovskite phases with $n=2, 3, 4$, and ∞ , respectively. By comparing the intensity of the absorption curves, it can be

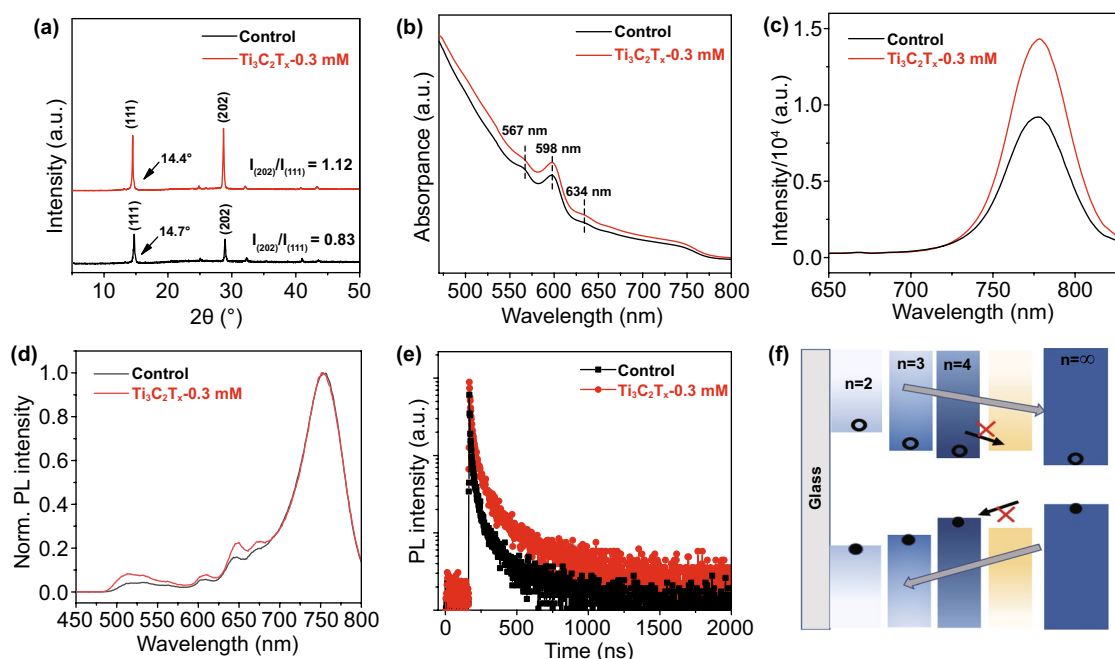


Fig. 4 **a** XRD patterns, **b** UV/Vis absorption spectra, **c**, **d** PL spectra excited from front and back side and **e** time-resolved PL spectrums for the control and optimized $\text{Ti}_3\text{C}_2\text{T}_x$ -doping perovskite films (on ITO substrates). **f** Illustration of band structure of 2D perovskite film

seen that the $\text{Ti}_3\text{C}_2\text{T}_x$ -0.3 mM perovskite films exhibited a stronger absorption at all wavelengths, due to enhanced light scattering and reflection [48]. The direct optical bandgaps of the control and $\text{Ti}_3\text{C}_2\text{T}_x$ -0.3 mM perovskite films (Fig. S6) remained almost unchanged.

To further illustrate the multiphase distribution in the 2D perovskite film and the effects of $\text{Ti}_3\text{C}_2\text{T}_x$ -0.3 mM doping, PL spectra under front (film) and back (ITO) side excitations are shown in Fig. 4c, d. Upon front excitation, only one individual peak appeared in the spectra of both control and $\text{Ti}_3\text{C}_2\text{T}_x$ -0.3 mM films, owing to the region of PL light excitation being confined close to the surface of the perovskite layer. According to previous reports [49], separate peaks originate from large- n phases on the surface of 2D perovskite films. Moreover, the stronger emission intensity of the $\text{Ti}_3\text{C}_2\text{T}_x$ -0.3 mM films compared with that of the control reflects the suppression of non-radiative recombination, which can be related to the passivation of defects, in accordance with the SEM findings. Upon back excitation, we could observe phases with different small- n values, which is consistent with previous reports [46]. Surprisingly, $\text{Ti}_3\text{C}_2\text{T}_x$ -0.3 mM led to a slight peak enhancement in the small- n phase of the bottom film, which can be explained by the kinetics of film growth after $\text{Ti}_3\text{C}_2\text{T}_x$ -doping [18]. Due

to the low solubility in the perovskite precursor, $\text{Ti}_3\text{C}_2\text{T}_x$ may largely precipitate at the bottom of the film during spin coating and annealing, acting as a nucleation center for the lower- n phases within the bulk, which would increase nucleation of the small- n phases and ultimately favor a uniform phase distribution [50]. The enhancement in J_{sc} is largely due to this feature. Liu et al. [51] proposed that the $n = \infty$ phase is predominantly distributed at the top of the film, with $n = 2, 3, 4$, and ∞ phases coexisting in the middle, and only small- n phases present at the bottom of 2D perovskite films. However, the small- n phases existing in the intermediate mixing region can act as shallow traps in 2D bulk perovskites [51, 52], blocking charge separation and transport, and ultimately greatly affecting the J_{sc} of the devices. $\text{Ti}_3\text{C}_2\text{T}_x$ doping can suppress the density of these shallow traps and thus extend the lifetime of the carriers, as shown in Fig. 4e. The time-resolved PL spectrums show that the $\text{Ti}_3\text{C}_2\text{T}_x$ -0.3 mM film exhibited longer average lifetimes compared to the control film. The fit formula and relevant parameters of carrier lifetimes are summarized in Table S2. This finding is a good indication that the addition of $\text{Ti}_3\text{C}_2\text{T}_x$ can inhibit non-radiative recombination losses and thus enhance J_{sc} . The sequential spatial distribution in the order of n values is illustrated in Fig. 4f. With an ordered

distribution of n values, photogenerated excitons are efficiently dissociated into electrons and holes, shifted in opposite directions, and eventually collected by the electrode.

3.5 Carrier Dynamics

Current density versus incident light intensity plots were used to illustrate the dynamics of carrier recombination in devices, which follows the relationship $J_{sc} \propto I^\alpha$, as shown in Fig. 5a. The $Ti_3C_2T_x$ -0.3 mM device shows a relationship more closely related to the ideal factor ($\alpha = 1$) on a double-logarithmic scale, with a value of 0.961, compared to a value of 0.953 for the control device; this indicates a lower degree of bimolecular recombination [25], which may be largely attributed to the reduction in trap density, consistent with the SEM observations. In order to quantify the passivation effect of the device upon addition of $Ti_3C_2T_x$ nanosheets,

we measured dark I - V curves of devices with $SnO_2/2D$ perovskite/PCBM/Ag structure, as shown in Fig. 5c, d. The relevant details of the calculation can be seen in the supporting information. The calculated defect density of the $Ti_3C_2T_x$ -incorporating devices was $0.89 \times 10^{15} \text{ cm}^{-3}$, which is lower than that of the control device ($1.16 \times 10^{15} \text{ cm}^{-3}$), suggesting an improved quality of 2D perovskite film after $Ti_3C_2T_x$ -doping.

Subsequently, we examined the characteristics of both devices through electrochemical impedance spectroscopy (EIS) measurements and the Nyquist plots shown in Fig. 5b, with the equivalent circuit model displayed in the inset. Here, R_s represents the series resistance, which primarily reflects the electrical contacts, wires, and sheet resistance of the electrodes [53]. The charge-transfer properties at the interface are reflected by the charge-transfer resistance (R_{tr}), whereas R_{rec} is related to the recombination of the carriers [54]. It is clear that the R_s values of

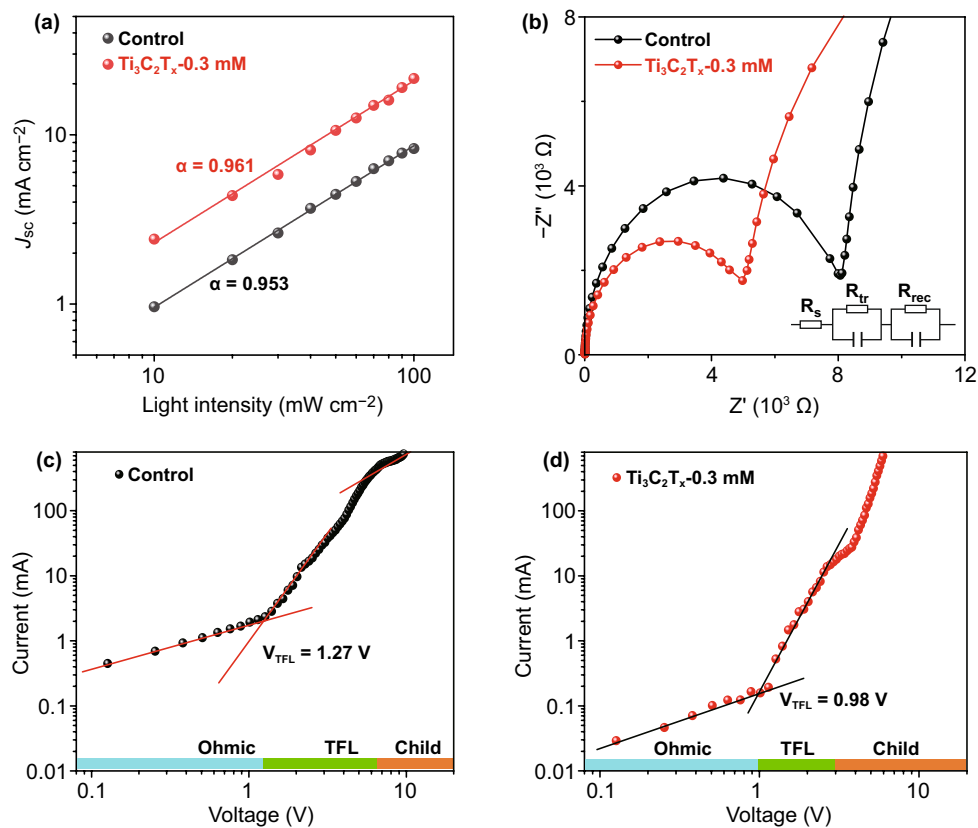


Fig. 5 **a** J_{sc} versus light intensity and **b** Nyquist plots of EIS with the equivalent circuit for the control and optimized $Ti_3C_2T_x$ -doping perovskite devices. **c**, **d** I - V curves of the electron-only devices under dark based on the control and optimized $Ti_3C_2T_x$ -doping

the two devices were similar. However, there was a significant variation in the R_{tr} value upon $Ti_3C_2T_x$ doping. Obviously, the $Ti_3C_2T_x$ -0.3 mM sample displayed a lower R_{tr} value, indicating an optimal charge transfer, which can be explained in terms of the charge-transfer speed at the perovskite/ETL and perovskite/HTL interfaces. The apparent negative relationship between the R_{tr} value and $Ti_3C_2T_x$ doping implies that the charge transport at the surface greatly affects the J_{sc} and PCE values.

3.6 Devices Stability

In contrast to 3D perovskites, excellent stability has always been a characteristic feature of 2D perovskites [12, 55]. The unencapsulated perovskite devices were placed in an environment with $55 \pm 5\%$ humidity to monitor their long-term stability. After a certain period of time, the devices were re-exposed to standard light intensity to test their PCE values, as shown in Fig. 6. Overall, the 2D perovskite devices exhibited superior long-term stability in comparison with their 3D counterparts, with almost no degradation after 300 h. Satisfactorily, the $Ti_3C_2T_x$ -based devices maintained 80% of their original PCE value after up to 750 h, while the PCE of the control devices was reduced to 40% of the initial value after 700 h of storage. In addition, we examined the thermal stability of 2D perovskite films with/without the presence of $Ti_3C_2T_x$. Figure S7 shows the dependence of absorption intensity reflecting the degradation of 2D perovskite films on continuous heating at $150^\circ C$ in a N_2 -filled glove box. Compared to $Ti_3C_2T_x$ -0 mM perovskite film (original film), $Ti_3C_2T_x$ -0.3 mM perovskite film remains almost unchanged after 12 h in the absorption

intensity. After 48 h of thermal aging test, the absorption intensity of $Ti_3C_2T_x$ -0 mM perovskite film is substantially decreased, whereas no serious decrease in the absorbance was observed in $Ti_3C_2T_x$ -0.3 mM perovskite films. This result indicates that the presence of $Ti_3C_2T_x$ improves the thermal stability of 2D perovskite films. It has been reported that when the perovskite devices are exposed to water molecules in the air or continuous high temperature, the additives in Spiro-OMeTAD will diffuse into the perovskite film and the organic components will escape from film to damage the film structure, and eventually leading to film decomposition [56]. The $Ti_3C_2T_x$ -containing perovskite precursor solution is spin-coated onto the substrate, and $Ti_3C_2T_x$ in the bulk phase will induce the protonation with CH_3NH_3 (MA), because the surface fluorine terminal groups of $Ti_3C_2T_x$ have a strong interaction with hydrogen atoms of MA [45], which results in the superior crystallinity of the $Ti_3C_2T_x$ -doped perovskite films (Fig. 4a). In addition, a portion of the $Ti_3C_2T_x$ not inserted into the perovskite lattice will stay at the crystal boundary to passivate defects, as shown in Fig. 3b. Besides, the improved stability of the $Ti_3C_2T_x$ -based samples compared to the control sample can also be attributed to the van der Waals interaction that significantly stabilize the framework of 2D perovskite films, resulting in highly oriented crystals with fewer detrimental defects. Moreover, previous studies suggest that species with low- n values in the perovskite layer will produce a passivated layer blocking further degradation [12, 57]. Therefore, the incorporation of $Ti_3C_2T_x$ in perovskite devices provides joint consequence of above effects leading to a higher long-term stability.

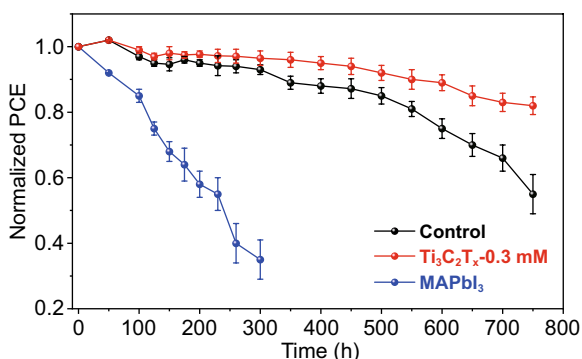


Fig. 6 Stability of MAPbI₃-based, control, and $Ti_3C_2T_x$ -doping devices without sealing at air atmosphere with humidity of $55 \pm 5\%$

4 Conclusion

In summary, we have shown that a moderate doping level of $Ti_3C_2T_x$ nanosheets can greatly improve the quality of 2D perovskite $(BA)_2(MA)_4Pb_3I_{16}$ films as well as the photovoltaic performance of the corresponding device, with an increase in PCE from 13.69 to 15.71%, owing to a significant increase in current. The superiority of the $Ti_3C_2T_x$ -doped devices is mainly attributed to the intensified crystallinity, vertically oriented growth, and homogeneous phase distribution in the thin film, which ultimately facilitates charge transport. In addition, the $Ti_3C_2T_x$ nanosheets-doped devices

exhibit a relatively higher humidity stability than the raw devices, owing to the better crystallinity and passivation effect of perovskite films. This work provides an effective strategy for improving the performance of 2D perovskite films and further expands the applications of $\text{Ti}_3\text{C}_2\text{T}_x$ in photovoltaics.

Acknowledgements Xin Jin and Lin Yang contribute equally to this work. This work was supported by the National Natural Science Foundation of China (No. 11974129 to X.-F. W.) and “the Fundamental Research Funds for the Central Universities, Jilin University.”

Open Access This article is licensed under a Creative Commons Attribution 4.0 International License, which permits use, sharing, adaptation, distribution and reproduction in any medium or format, as long as you give appropriate credit to the original author(s) and the source, provide a link to the Creative Commons licence, and indicate if changes were made. The images or other third party material in this article are included in the article’s Creative Commons licence, unless indicated otherwise in a credit line to the material. If material is not included in the article’s Creative Commons licence and your intended use is not permitted by statutory regulation or exceeds the permitted use, you will need to obtain permission directly from the copyright holder. To view a copy of this licence, visit <http://creativecommons.org/licenses/by/4.0/>.

Supplementary Information The online version contains supplementary material available at <https://doi.org/10.1007/s40820-021-00602-w>.

References

1. S.D. Stranks, G.E. Eperon, G. Grancini, C. Menelaou, M.J.P. Alcocer et al., Electron-hole diffusion lengths exceeding 1 micrometer in an organometal trihalide perovskite absorber. *Science* **342**(6156), 341–344 (2013). <https://doi.org/10.1126/science.1243982>
2. G.C. Xing, N. Mathews, S.Y. Sun, S.S. Lim, Y.M. Lam et al., Long-range balanced electron- and hole-transport lengths in organic–inorganic $\text{CH}_3\text{NH}_3\text{PbI}_3$. *Science* **342**(6156), 344–347 (2013). <https://doi.org/10.1126/science.1243167>
3. C.T. Zuo, H.J. Bolink, H.W. Han, J.S. Huang, D. Cahen et al., Advances in perovskite solar cells. *Adv. Sci.* **3**(7), 1500324 (2016). <https://doi.org/10.1002/adv.201500324>
4. T.M. Brenner, D.A. Egger, L. Kronik, G. Hodes, D. Cahen, Hybrid organic–inorganic perovskites: low-cost semiconductors with intriguing charge-transport properties. *Nat. Rev. Mater.* **1**(1), 16 (2016). <https://doi.org/10.1038/natrevmats.2015.7>
5. S.-W. Lee, S. Bae, D. Kim, H.-S. Lee, Historical analysis of high-efficiency, large-area solar cells: toward upscaling of perovskite solar cells. *Adv. Mater.* (2020). <https://doi.org/10.1002/adma.202002202>
6. M.A. Green, E.D. Dunlop, D.H. Levi, J. Hohl-Ebinger, M. Yoshita et al., Solar cell efficiency tables (version 55). *Prog. Photovolt.* **28**(1), 3–15 (2020). <https://doi.org/10.1002/pip.3228>
7. P. Buin, J.X. Pietsch, O. Xu, A.H.I. Voznyy et al., Materials processing routes to trap-free halide perovskites. *Nano Lett.* **14**(11), 6281–6286 (2014). <https://doi.org/10.1021/nl502612m>
8. I.C. Smith, E.T. Hoke, D. Solis-Ibarra, M.D. McGehee, H.I. Karunadasa, A layered hybrid perovskite solar-cell absorber with enhanced moisture stability. *Angew. Chem. Int. Ed.* **53**(42), 11232–11235 (2014). <https://doi.org/10.1002/anie.201406466>
9. H.H. Tsai, W.Y. Nie, J.C. Blancon, C.C.S. Toumpos, R. Asadpour et al., High-efficiency two-dimensional Ruddlesden–Popper perovskite solar cells. *Nature* **536**(7616), 312–316 (2016). <https://doi.org/10.1038/nature18306>
10. S. Chen, G.Q. Shi, Two-dimensional materials for halide perovskite-based optoelectronic devices. *Adv. Mater.* **29**(24), 1605448 (2017). <https://doi.org/10.1002/adma.201605448>
11. L.L. Mao, C.C. Stoumpos, M.G. Kanatzidis, Two-dimensional hybrid halide perovskites: principles and Promises. *J. Am. Chem. Soc.* **141**(3), 1171–1190 (2019). <https://doi.org/10.1021/jacs.8b10851>
12. L.N. Quan, M.J. Yuan, R. Comin, O. Voznyy, E.M. Beauregard et al., Ligand-stabilized reduced-dimensionality perovskites. *J. Am. Chem. Soc.* **138**(8), 2649–2655 (2016). <https://doi.org/10.1021/jacs.5b11740>
13. P.R. Cheng, P.J. Wang, Z. Xu, X.G. Jia, Q.L. Wei et al., Ligand-size related dimensionality control in metal halide perovskites. *ACS Energy Lett.* **4**(8), 1830–1838 (2019). <https://doi.org/10.1021/acseenergylett.9b01100>
14. X. Xiao, J. Dai, Y.J. Fang, J.J. Zhao, X.P. Zheng et al., Suppressed ion migration along the in-plane direction in layered perovskites. *ACS Energy Lett.* **3**(3), 684–688 (2018). <https://doi.org/10.1021/acseenergylett.8b00047>
15. P. Ortiz-Cervantes, D. Carmona-Monroy, Solis-Ibarra, two-dimensional halide perovskites in solar cells: 2D or not 2D? *Chemsuschem* **12**(8), 1560–1575 (2019). <https://doi.org/10.1002/cssc.201802992>
16. H.H. Tsai, R. Asadpour, J.C. Blancon, C.C. Stoumpos, J. Even et al., Design principles for electronic charge transport in solution-processed vertically stacked 2D perovskite quantum wells. *Nat. Commun.* **9**(9), 2130 (2018). <https://doi.org/10.1038/s41467-018-04430-2>
17. X.Q. Zhang, G. Wu, W.F. Fu, M.C. Qin, W.T. Yang et al., Orientation regulation of phenylethylammonium cation based 2D perovskite solar cell with efficiency higher than 11%. *Adv. Energy Mater.* **8**(14), 9 (2018). <https://doi.org/10.1002/aenm.201702498>
18. J.S. Shi, Y.R. Gao, X. Gao, Y. Zhang, J.J. Zhang et al., Fluorinated low-dimensional Ruddlesden–Popper perovskite solar cells with over 17% power conversion efficiency and improved stability. *Adv. Mater.* **31**(37), 1901673 (2019). <https://doi.org/10.1002/adma.201901673>



19. S.Q. Tan, N. Zhou, Y.H. Chen, L. Li, G.L. Liu et al., Effect of high dipole moment cation on layered 2D organic-inorganic halide perovskite solar cells. *Adv. Energy Mater.* **9**(5), 1803024 (2019). <https://doi.org/10.1002/aenm.201803024>
20. W. Chen, L.M. Xu, X.Y. Feng, J.S. Jie, Z.B. He, Metal acetylacetonate series in interface engineering for full low-temperature-processed, high-performance, and stable planar perovskite solar cells with conversion efficiency over 16% on 1 cm² scale. *Adv. Mater.* **29**(16), 1603923 (2017). <https://doi.org/10.1002/adma.201603923>
21. J. Qiu, Y.T. Zheng, Y.D. Xia, L.F. Chao, Y.H. Chen et al., Rapid crystallization for efficient 2D Ruddlesden–Popper (2DRP) perovskite solar cells. *Adv. Funct. Mater.* **29**(47), 1806831 (2019). <https://doi.org/10.1002/adfm.201806831>
22. X. Zhang, X.D. Ren, B. Liu, R. Munir, X.J. Zhu et al., Stable high efficiency two-dimensional perovskite solar cells via cesium doping. *Energy Environ. Sci.* **10**(10), 2095–2102 (2017). <https://doi.org/10.1039/c7ee01145h>
23. G.B. Wu, X. Li, J.Y. Zhou, J.Q. Zhang, X.N. Zhang et al., Fine multi-phase alignments in 2D perovskite solar cells with efficiency over 17% via slow post-annealing. *Adv. Mater.* **31**(42), 1903889 (2019). <https://doi.org/10.1002/adma.201903889>
24. J. Zhang, J.J. Qin, M.S. Wang, Y.J. Bai, H. Zou et al., Uniform permutation of quasi-2D perovskites by vacuum poling for efficient, high-fill-factor solar cells. *Joule* **3**(12), 3061–3071 (2019). <https://doi.org/10.1016/j.joule.2019.09.020>
25. H.T. Lai, B. Kan, T.T. Liu, N. Zheng, Z.Q. Xie et al., Two-dimensional Ruddlesden–Popper perovskite with nanorod-like morphology for solar cells with efficiency exceeding 15%. *J. Am. Chem. Soc.* **140**(37), 11639–11646 (2018). <https://doi.org/10.1021/jacs.8b04604>
26. X.M. Lian, J.H. Chen, R.L. Fu, T.K. Lau, Y.Z. Zhang et al., An inverted planar solar cell with 13% efficiency and a sensitive visible light detector based on orientation regulated 2D perovskites. *J. Mater. Chem. A* **6**(47), 24633–24640 (2018). <https://doi.org/10.1039/c8ta08203k>
27. Z.Y. Xu, D. Lu, F. Liu, H.T. Lai, X.J. Wan et al., Phase distribution and carrier dynamics in multiple-ring aromatic spacer-based two-dimensional Ruddlesden–Popper perovskite solar cells. *ACS Nano* **14**(4), 4871–4881 (2020). <https://doi.org/10.1021/acsnano.0c00875>
28. C.T. Zuo, A. Scully, D. Yak, W.L. Tan, X.C. Jiao et al., Self-assembled 2D perovskite layers for efficient printable solar cells. *Adv. Energy Mater.* **9**(4), 1803258 (2019). <https://doi.org/10.1002/aenm.201803258>
29. A. Zuo, T.W. Scully, F. Liang, K.G. Zheng et al., Crystallisation control of drop-cast quasi-2D/3D perovskite layers for efficient solar cells. *Commun. Mater.* **1**, 33 (2020). <https://doi.org/10.1038/s43246-020-0036-z>
30. X. Li, G. Wu, M. Wang, B. Yu, J. Zhou et al., Water-assisted crystal growth in quasi-2D perovskites with enhanced charge transport and photovoltaic performance. *Adv. Energy Mater.* **10**(37), 2001832 (2020). <https://doi.org/10.1002/aenm.202001832>
31. L.G. Gao, F. Zhang, X.H. Chen, C.X. Xiao, B.W. Larson et al., Enhanced charge transport by incorporating formamidinium and cesium cations into two-dimensional perovskite solar cells. *Angew. Chem. Int. Ed.* **58**(34), 11737–11741 (2019). <https://doi.org/10.1002/anie.201905690>
32. F. Zhang, D.H. Kim, H.P. Lu, J.S. Park, B.W. Larson et al., Enhanced charge transport in 2D perovskites via fluorination of organic cation. *J. Am. Chem. Soc.* **141**(14), 5972–5979 (2019). <https://doi.org/10.1021/jacs.9b00972>
33. X. Zhang, R. Munir, Z. Xu, Y.C. Liu, H. Tsai et al., Phase transition control for high performance Ruddlesden–Popper perovskite solar cells. *Adv. Mater.* **30**(21), 1707166 (2018). <https://doi.org/10.1002/adma.201707166>
34. J. Hu, I.W.H. Oswald, S.J. Stuard, M.M. Nahid, N.H. Zhou et al., Synthetic control over orientational degeneracy of spacer cations enhances solar cell efficiency in two-dimensional perovskites. *Nat. Commun.* **10**, 1276 (2019). <https://doi.org/10.1038/s41467-019-08980-x>
35. M. Zhou, C.B. Fei, J.S. Sarmiento, H. Wang, Manipulating the phase distributions and carrier transfers in hybrid quasi-two-dimensional perovskite films. *Sol. RRL* **3**(4), 1800359 (2019). <https://doi.org/10.1002/solr.201800359>
36. Q. Jiang, Y. Zhao, X.W. Zhang, X.L. Yang, Y. Chen et al., Surface passivation of perovskite film for efficient solar cells. *Nat. Photon.* **13**(7), 460 (2019). <https://doi.org/10.1038/s41566-019-0398-2>
37. M. Alhabeab, K. Maleski, B. Anasori, P. Lelyukh, L. Clark et al., Guidelines for synthesis and processing of two-dimensional titanium carbide (Ti₃C₂T_x MXene). *Chem. Mater.* **29**(18), 7633–7644 (2017). <https://doi.org/10.1021/acs.chemmater.7b02847>
38. M. Ghidui, M.R. Lukatskaya, M.Q. Zhao, Y. Gogotsi, M.W. Barsoum, Conductive two-dimensional titanium carbide “clay” with high volumetric capacitance. *Nature* **516**(7529), 78–81 (2014). <https://doi.org/10.1038/nature13970>
39. Y. Dall’Agnese, B. Dall’Agnese, W. Anasori, S. Sugimoto, Mori, Oxidized Ti₃C₂ MXene nanosheets for dye-sensitized solar cells. *New J. Chem.* **42**(20), 16446–16450 (2018). <https://doi.org/10.1039/c8nj03246g>
40. H.C. Fu, V. Ramalingam, H. Kim, C.H. Lin, X.S. Fang et al., MXene-contacted silicon solar cells with 11.5% efficiency. *Adv. Energy Mater.* **9**(22), 1900180 (2019). <https://doi.org/10.1002/aenm.201900180>
41. Z. Yu, W. Feng, W. Lu, B. Li, H. Yao et al., MXenes with tunable work functions and their application as electron- and hole-transport materials in non-fullerene organic solar cells. *J. Mater. Chem. A* **7**(18), 11160–11169 (2019). <https://doi.org/10.1039/c9ta01195a>
42. L. Yang, C. Dall’Agnese, Y. Dall’Agnese, G. Chen, Y. Gao et al., Surface-modified metallic Ti₃C₂T_x MXene as electron transport layer for planar heterojunction perovskite solar cells. *Adv. Funct. Mater.* **29**(46), 1905694 (2019). <https://doi.org/10.1002/adfm.201905694>
43. L. Yang, Y. Dall’Agnese, K. Hantanasirisakul, C.E. Shuck, K. Maleski et al., SnO₂–Ti₃C₂ MXene electron transport layers for perovskite solar cells. *J. Mater. Chem. A* **7**(10), 5635–5642 (2019). <https://doi.org/10.1039/c8ta12140k>

44. L.S. Huang, X.W. Zhou, R. Xue, P.F. Xu, S.L. Wang et al., Low-temperature growing anatase TiO₂/SnO₂ multi-dimensional heterojunctions at MXene conductive network for high-efficient perovskite solar cells. *Nano-Micro Lett.* **12**(1), 19 (2020). <https://doi.org/10.1007/s40820-020-0379-5>
45. Z.L. Guo, L.G. Gao, Z.H. Xu, S. Teo, C. Zhang et al., High electrical conductivity 2D MXene serves as additive of perovskite for efficient solar cells. *Small* **14**(47), 1802738 (2018). <https://doi.org/10.1002/sml.201802738>
46. N. Zhou, Y. Shen, L. Li, S. Tan, N. Liu et al., Exploration of crystallization kinetics in quasi two-dimensional perovskite and high performance solar cells. *J. Am. Chem. Soc.* **140**(1), 459–465 (2018). <https://doi.org/10.1021/jacs.7b11157>
47. Y. Cao, N.N. Wang, H. Tian, J.S. Guo, Y.Q. Wei et al., Perovskite light-emitting diodes based on spontaneously formed submicrometre-scale structures. *Nature* **562**(7726), 249–253 (2018). <https://doi.org/10.1038/s41586-018-0576-2>
48. Z.G. Xiao, Q.F. Dong, C. Bi, Y.C. Shao, Y.B. Yuan et al., Solvent annealing of perovskite-induced crystal growth for photovoltaic-device efficiency enhancement. *Adv. Mater.* **26**(37), 6503–6509 (2014). <https://doi.org/10.1002/adma.201401685>
49. J. Liu, J. Leng, K. Wu, J. Zhang, S. Jin, Observation of internal photoinduced electron and hole separation in hybrid two-dimensional perovskite films. *J. Am. Chem. Soc.* **139**(4), 1432–1435 (2017). <https://doi.org/10.1021/jacs.6b12581>
50. B.R. Wygant, G.T. Geberth, A.Z. Ye, A. Dolocan, D.E. Cotton et al., Moisture-driven formation and growth of quasi-2D organolead halide perovskite crystallites. *ACS Appl. Energy Mater.* **3**(7), 6280–6290 (2020). <https://doi.org/10.1021/acsaelm.0c00423>
51. N. Liu, P.F. Liu, H.X. Ren, H.P. Xie, N. Zhou et al., Probing phase distribution in 2D perovskites for efficient device design. *ACS Appl. Mater. Interfaces* **12**(2), 3127–3133 (2020). <https://doi.org/10.1021/acsami.9b17047>
52. A.H. Proppe, R. Quintero-Bermudez, H. Tan, O. Voznyy, S.O. Kelley et al., Synthetic control over quantum well width distribution and carrier migration in low-dimensional perovskite photovoltaics. *J. Am. Chem. Soc.* **140**(8), 2890–2896 (2018). <https://doi.org/10.1021/jacs.7b12551>
53. R. Wu, J. Yao, S. Wang, X. Zhou, Q. Wang et al., Ultracompact, well-packed perovskite flat crystals: preparation and application in planar solar cells with high efficiency and humidity tolerance. *ACS Appl. Mater. Interfaces* **11**(12), 11283–11291 (2019). <https://doi.org/10.1021/acsami.8b17300>
54. Y. Ma, N. Wei, Q. Wang, C. Wu, W. Zeng et al., Ultrathin PEDOT:PSS/rGO aerogel providing tape-like self-healable electrode for sensing space electric field with electrochemical mechanism. *Adv. Electron. Mater.* **5**(12), 1900637 (2019). <https://doi.org/10.1002/aelm.201900637>
55. H.Y. Zheng, G.Z. Liu, L.Z. Zhu, J.J. Ye, X.H. Zhang et al., The effect of hydrophobicity of ammonium salts on stability of quasi-2D perovskite materials in moist condition. *Adv. Energy Mater.* **8**(21), 1800051 (2018). <https://doi.org/10.1002/aenm.201800051>
56. H.Y. Zheng, W.W. Wu, H.F. Xu, F.C. Zheng, G.Z. Liu et al., Self-additive low-dimensional Ruddlesden–Popper perovskite by the incorporation of glycine hydrochloride for high-performance and stable solar cells. *Adv. Funct. Mater.* **30**(15), 2000034 (2020). <https://doi.org/10.1002/adfm.202000034>
57. B.R. Wygant, A.Z. Ye, A. Dolocan, Q. Vu, D.M. Abbot et al., Probing the degradation chemistry and enhanced stability of 2D organolead halide perovskites. *J. Am. Chem. Soc.* **141**(45), 18170–18181 (2019). <https://doi.org/10.1021/jacs.9b08895>

